Comparison of real-time phase-reconstruction methods in temporal speckle-pattern interferometry

Pablo Etchepareborda,[1,*] Arturo Bianchetti,[1] Francisco E. Veiras,[2] Ana Laura Vadnjal,[1] Alejandro Federico,[1] and Guillermo H. Kaufmann[3]

[1]*Electrónica e Informática, Instituto Nacional de Tecnología Industrial, P.O. Box B1650WAB, B1650KNA San Martín, Argentina*
[2]*Laboratorio de Sistemas Líquidos, GLOmAe, Departamento de Física, Facultad de Ingeniería, Universidad de Buenos Aires, Avenida Paseo Colón 850, Ciudad Autónoma de Buenos Aires C1063ACV, Argentina*
[3]*Instituto de Física Rosario y Centro Internacional Franco Argentino de Ciencias de la Información y de Sistemas, Ocampo y Esmeralda, S2000EZP Rosario, Argentina*
*Corresponding author: pabloe@inti.gov.ar

Three real-time methods for object-phase recovery are implemented and compared in temporal speckle-pattern interferometry. Empirical mode and intrinsic time-scale decompositions are used and compared as real-time non-stationary and nonlinear filtering techniques for the extraction of the spatio-temporal evolution of the object phase. The proposed real-time methods avoid the application of the Hilbert transform and improve the accuracy of the measurement by filtering under-modulated pixels using Delaunay triangulation. The performance of the proposed methods is evaluated by comparing phase-recovery accuracy and computation time by means of numerical simulations and experimental data obtained from common and simultaneous $\pi/2$ phase-shifting heterodyne interferometry. © 2015 Optical Society of America

1. INTRODUCTION

Speckle metrology techniques have been widely used for displacement measurements due to their simple and adaptable experimental arrangement. Particularly, several methods were implemented for quality assessment in the development of microstructured devices having optically rough surfaces and their optimization based on *in situ* prototype mechanical testing [1]. The measurement of deformations of micromechanical parts under mechanical, thermal, magnetic, or electrostatic loads allow us to confirm analytical and finite element models, access material, and device properties, detect potential defects, and determine functionality and reliability performance of micro-electromechanical systems. Digital holography and digital speckle-pattern interferometry (DSPI) assisted by image-processing techniques are used to reconstruct the spatio-temporal information of the object optical phase concealed in speckle-pattern images in order to measure the out-of-plane or in-plane nano-metric displacements of microstructures [2]. Furthermore, the introduction of real-time optical inspection techniques allows us to characterize its dynamic properties by offering an extra measurement capability for the development and the control of the manufacturing process.

In other multidisciplinary fields such as microfluidics applications, it is well known that the use of holographic optical tweezers provides the ability to move microstructures throughout the sample volume and the use of real-time inspection techniques gain an effective way of visualization and tracking. Digital holographic microscopy has been widely used for real-time monitoring of fluid flow over the volume of a microfluidic channel [3] and also it has been frequently implemented for real-time metrology [4]. However, the use of the temporal speckle-pattern interferometry (TSPI) technique avoids numerical field reconstruction from an intermediate hologram and the 2D phase unwrapping, which are inconvenient for a real-time visualization of continuous displacement fields. Spatial-phase shifting (SPS) is another technique for fast phase reconstruction in DSPI that was effectively used for online stroboscopic inspection of dynamic processes [5] and real-time quantitative phase imaging of biological samples [6]. In SPS a phase-shifting algorithm is implemented with the intensities of neighboring pixels taken in the direction of an introduced spatial fringe pattern that provides a constant phase shift between the considered pixels. Thus the processing of two images corresponding to different

states of the specimen obtains two phase maps that, by means of a subtraction, quantitatively describe the underlying deformation. However, SPS might cause the loss of some high-frequency information due to the background filter procedure; it also requires a costly post-processing of 2D unwrapping and is highly dependent on the spatial properties of the speckle field and the fringe spacing of the introduced spatial carrier. In TSPI the phase-reconstruction process is performed temporarily for each pixel by analyzing the correspondent 1D signal of the temporal history of the acquired intensity. Therefore, a simple 1D unwrapping procedure is used and the noise of neighboring pixels does not affect the measurement. Also, this temporal analysis has no special requirement for the spatial properties of the bias intensity pattern regarding the spacing of fringes or the mean speckle size and presents low dependence with the beam intensity ratio or visibility of modulation [7]. Burke and Helmers assert that temporal analysis usually works with a mean speckle size of approximately 1 pixel, which is confirmed by our assessment. They also cited works in which the temporal analysis even allows performance of DSPI measurements with images having a mean speckle size lower (or higher) than 1 pixel. In addition, the temporal analysis approach considerably extends the displacement measurement range as the spatial correlation length of the speckle pattern has no effects on the results [8].

A real-time DSPI system for detecting sub-surface delamination cracks in carbon-fiber composite panels was developed by directly extending a standard four-frame temporal phase shifting (TPS) algorithm [9]. However, the phase to be measured is assumed constant during the acquisition of the frames corresponding to a single state of deformation and should not be used carelessly in the inspection of dynamic deformations, even more so if the temporal decorrelation of the speckle field forces the reference instant to be close in time to the measuring instant. Unlike the temporal analysis based on TPS, which possesses an enhanced sensitivity for vibration and mechanical instabilities of the experimental setup, TSPI is essentially suitable to measure the transient deformations of continuously deforming objects with low complexity and low-cost optical setup [10].

In TSPI the spatial intensity distribution $I(t)$ measured at the CCD sensor is described by the two-beam interferometry equation $I(t) = I_0(t) + I_M(t) \cos[\Delta\phi(t)]$, where $I_0(t)$ is the background intensity, $I_M(t)$ is the modulation intensity, and $\Delta\phi(t) = \phi_o - \phi_r(t)$ is the phase difference between the phase of the reference arm $\phi_r(t)$ and the object phase $\phi_o(t)$ to be recovered. Note that the position of the analyzed pixel in the horizontal and vertical directions was intentionally omitted in this equation. A temporal carrier is introduced in $\phi_r(t)$ to split the modulation intensity term and to make possible the detection of the absolute sign of the object-phase evolution. Phase-recovery methods exploit different properties of the signal $I(t)$ intending to isolate the modulated intensity term while removing the presence of the background intensity for object-phase recovery. The Fourier transform (FT) approach is usually used and then bandpass filtering is applied on the Fourier spectrum of the entire signal to obtain a complex signal with its phase equal to $\Delta\phi(t)$ [11]. Many other methods were proposed to improve the accuracy and robustness of offline phase

reconstruction by the use of a wavelet-transform based filter [12,13], the use of an analytic function obtained by means of a Hilbert transform [14], and the addition of an adaptive data-driven filtering based on the empirical mode decomposition (EMD) [15] to cope with intrinsic difficulties such as abrupt fluctuations of TSPI signals [16,17]. However, the mentioned phase-recovery approaches are unsuitable to obtain robust real-time measurements due to the computational complexity of the involved signal processing.

In this work we implement and compare three real-time phase-reconstruction methods that avoid the application of the Hilbert transform and 2D spatial-phase unwrapping procedures in a common TSPI optical setup. The proposed real-time methods are based on empirical mode and intrinsic time-scale decompositions of the interferometric signal and offer important advantages in the development of the measurement algorithms according to the state of the art. In addition, due to a recently proved convenience of implementing simultaneous $\pi/2$ phase-shifting (quadrature) heterodyne interferometry (SQHI) for removing the influence of the modulation intensity term from the analyzed interferograms and give higher accuracy [18], the performance of the tested real-time phase-reconstruction methods is also evaluated by measuring out-of-plane deformations of a piezoelectric disk composed by PZT subject to an exponentially decaying voltage signal.

2. DIGITAL FILTERING METHODS

A. Fourier Transform
The Fourier transform method is based on a bandpass filtering approach. In this method, a fast Fourier transform (FFT) digital algorithm is applied to the entire temporal evolution of the intensity signal in each pixel, and then the inverse FFT is used for recovering the object phase by analyzing the spectrum adequately filtered [11]. The center frequency of the bandpass filter is located at the temporal carrier frequency and the span is set verifying that the background intensity bandwidth is under the lower cutoff frequency of the filter. The bandwidth of the filter is always selected in order to assure a correct phase recovery for all pixels (note that the actual side band of the spectrum of the pixel intensity evolution is determined by the object-phase excursion and the sampling rate).

In real-time applications it is necessary to obtain a measurement before the entire signal is acquired and Fourier transformed. A dedicated digital filter must then be implemented for the application of the complex bandpass filtering process, and for that purpose we follow [19]. The analysis of the complex filtered signal has its phase equal to $\Delta\phi(t)$ and the known carrier $\phi_r(t)$ should be subtracted to obtain $\phi_o(t)$. In this work we implemented a complex tenth-order Butterworth filter for the analysis of numerical and experimental data.

B. Bivariate EMD
In the phase-recovery method named Bivariate EMD (BivEMD), the interferometric equation is rearranged by multiplying both sides of the equality by the complex phase term associated with the temporal carrier $\exp(i\phi_r)$ to get a new signal $z \equiv I \exp(i\phi_r)$ given by

$$z = I_0 e^{i\phi_r} + \frac{I_M}{2} e^{i\phi_o} + \frac{I_M}{2} e^{-i(\phi_o - 2\phi_r)}, \qquad (1)$$

where the spatio-temporal dependence was omitted for clarity [20]. At least two different characteristic time scales within the three terms at the right-hand side of Eq. (1) are immediately distinguished since the variations imposed by ϕ_o are much slower than the phase changes given by ϕ_r. BivEMD is applied on $z(t)$ to identify and separate the slower term in Eq. (1) corresponding to the object phase.

BivEMD is an extension of the EMD to decompose complex valued signals using the intuitive concept of a rotation trajectory in a 2D plane [21]. The BivEMD algorithm empirically decomposes the data as a set of superimposed rotating modes $c_j(t)$ and one trend or residue signal $r_J(t)$ with levels $1 \leq j \leq J$. This decomposition adaptively derives its own set of basic functions by extracting different rotating modes directly from the data where each mode can be linked to a particular time scale.

Bivariate intrinsic mode functions (BIMF) are defined by summing real signals at different directions similarly obtained as oscillating intrinsic mode functions (IMF) in EMD. The BivEMD algorithm *sifts* the complex rotating components $c_j(t)$ out from $z(t)$ in descending order of rotational speed until the expected amount of BIMFs is reached or no more rotating components can be driven from the last residue obtained. In order to extract the BIMF $c_j(t)$, the bivariate sifting process iteratively subtracts the slowest rotations from the residue $r_{j-1}(t)$ until they are no longer detectable or a fixed number of iterations is reached. At each sifting iteration, the center of the 3D tube that encloses the BIMF is extracted. This delineates a slowly rotating signal, which is found and subtracted. In order to find this tube the complex signal is projected on K different directions to obtain 1D real signals. The extrema of these signals are then detected to find upper and lower envelopes using a piecewise cubic Hermite interpolating polynomial (PCHIP). In this work we used four directions $K = 4$ with $k \in \{1, 2, \ldots, K\}$ rad defined by the angles $\phi_k \in \{0, \pi/2, \pi, 3\pi/2\}$ rad for the sifting operation $c_j(t) = \mathcal{S}[r_{j-1}(t)]$, which can be briefly formulated by means of the steps in the algorithm 1. In algorithm 1, $\Re$ is the real part of $\{\bullet\}$. This adaptive time scale decomposition allows us to properly select and sum the BIMFs that isolate the rotational term of $\phi_o(t)$ in Eq. (1). Subsequently, the object phase is recovered by means of the arc tan function.

Algorithm 1: *Complex sifting process using $K = 4$.*

Set $c_j(t) = r_{j-1}(t)$.
for $1 \leq k \leq K/2$ do
    project complex $c_j(t)$ on direction ϕ_k to get real
$p_k(t) = \Re\{e^{-i\phi_k} c_j(t)\}$.
    Apply EMD algorithm to $p_k(t)$ to get partial estimate in
direction ϕ_k, $s_k(t)$.
Compute new estimate. $c_j(t) = \frac{4}{K} \sum_{k=1}^{K/2} e^{i\phi_k} s_k(t)$.

Depending on the temporal variation of the object phase, the sampling rate, the frequency of the temporal carrier, and the bandwidth of the modulation intensity, the selection of the quantity of BIMFs to remove from the decomposition of $z(t)$ is determinant for the performance of the phase-reconstruction

method. In this work we show the results of extracting 1 and 2 BIMFs.

Several methods for extending the EMD to real-time applications were proposed based on a sliding window approach [22–24] and also by introducing complex filtering processes [25]. In this work we make use of a recent approach presented in [26] to avoid typical discontinuities of blockwise extracted modes by exploiting the locality of PCHIP for the estimation of envelopes during the sifting process. The occurrence of an extreme at the input signal starts a sifting iterative process over the segment of signal that contains the last five extremes as shown in Fig. 1. Specific boundary conditions (BC) of the initial value and first derivative are used to calculate the envelopes of the sifting process. The process is depicted for a generic signal in Fig. 2. The boundary conditions of the first sifting iteration are kept from the analysis of the previous segment of signal as

$$H_m(t_1) = \sum_{l=1}^{L} h_m^l(t_1), \qquad H_M(t_1) = \sum_{l=1}^{L} h_M^l(t_1), \qquad (2a)$$

$$\dot{H}_m(t_1) = \sum_{l=1}^{L} \dot{h}_m^l(t_1), \qquad \dot{H}_M(t_1) = \sum_{l=1}^{L} \dot{h}_M^l(t_1). \qquad (2b)$$

In Eq. (2) t_1 is the instant of the second extreme of the considered segment of signal, H_m the BC of total sum of lower envelopes, H_M the BC of total sum of upper envelopes, L the number of sifting iterations, $h_m^l(t)$ and $h_M^l(t)$ are the lower and upper envelopes at iteration l, and the dot operator $\dot{x}(t)$ indicates the first temporal derivative of $x(t)$. The sifting iterations $l > 1$ use null BC as shown in Fig. 2(b). We note that the
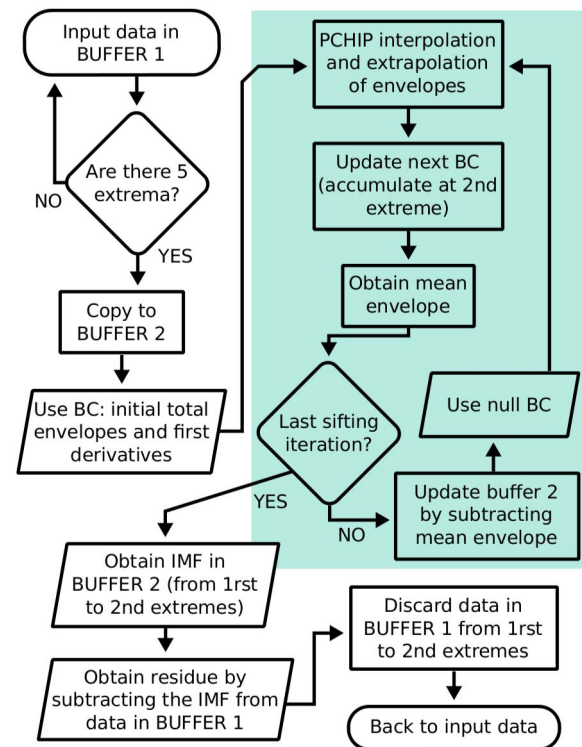

Fig. 1. Flowchart of the EMD algorithm using boundary conditions at first extreme for the upper and lower envelopes. The sifting iteration process is highlighted with a solid box.
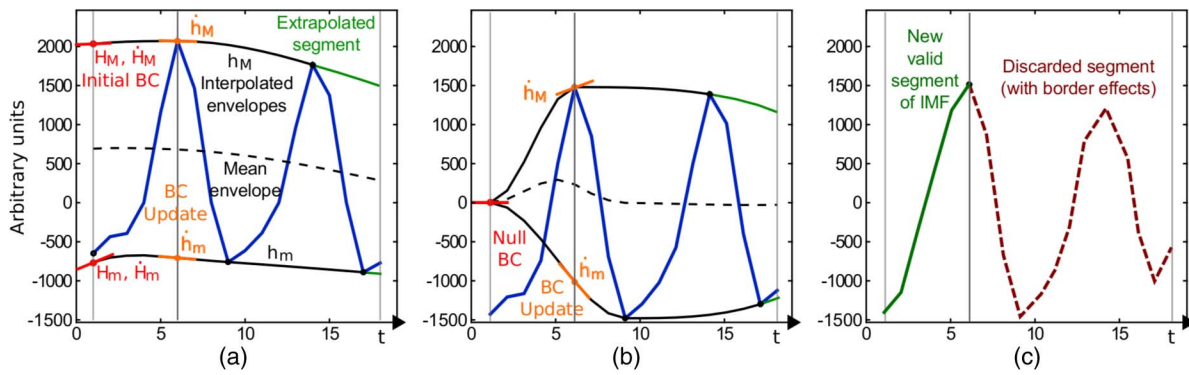
Fig. 2. Illustration of the EMD algorithm using boundary conditions at first extreme for the upper and lower envelopes for a generic signal. (a) First sifting iteration, (b) second sifting iteration, and (c) valid segment of extracted IMF.

PCHIP interpolation of $h_M^l(t)$ and $h_m^l(t)$ implement asymmetric numerical differentiation to obtain the first derivative of the envelope at the last maximum or minimum, respectively, and an extrapolation is required for every t higher than the last corresponding extreme. Due to those two sources of border effects, only the segment of the resulting signal in the time interval between the first and second extrema is held as the sifted IMF at iteration L.

The described approach obtains the first BIMF with a delay of three extremes [note that additional border effects can emerge when an extrapolation method and asymmetric numerical differentiation is used during the sifting process; see Fig. 2(a)]. The resulting BIMF is finally similar to the one obtained by the offline BivEMD. We note that much of the computational effort is dedicated to update segments of IMF that are removed when the sifting process stops.

In this work, we propose the implementation of a cascaded structure of sifting processors for an effective real-time TSPI phase-recovery method based on BivEMD. Two buffers are used to enqueue the real projections of $z(t)$ on the real and imaginary directions. Real-time EMD is applied on each projection. As shown in Fig. 3 the buffered data is served as input of the first of a sequence of sifting processors that pass their intermediate resulting IMF in cascade until the last sifting processor obtains the definitive IMF. That IMF is subtracted from the buffered signal to get the residue signal that can be also decomposed if needed. Each sifting processor is activated by the occurrence of an extreme in its corresponding input signal. The segment of signal containing the last six extremes and the derivative of the minimums and maxima envelopes at the first minimum and maximum are sufficient to find the mean envelope on the time interval between the second and third extremes, so that an intermediate resulting IMF is found and is the output to the next sifting processor. This proposed process is depicted for a generic signal in Fig. 4. We note that the resulting IMF is equal to the IMF obtained by the offline EMD algorithm as border effects are avoided through the entire process.

This approach presents a higher delay for obtaining the BIMF. However, the amount of the required interpolated values is considerably lower and the main computational effort is made in the interpolation process. Therefore, the results of this method are more suitable to real-time 2D phase recovery than

the method proposed in [26]. Furthermore, the BC are naturally obtained in the interpolation process with no extra operations needed.
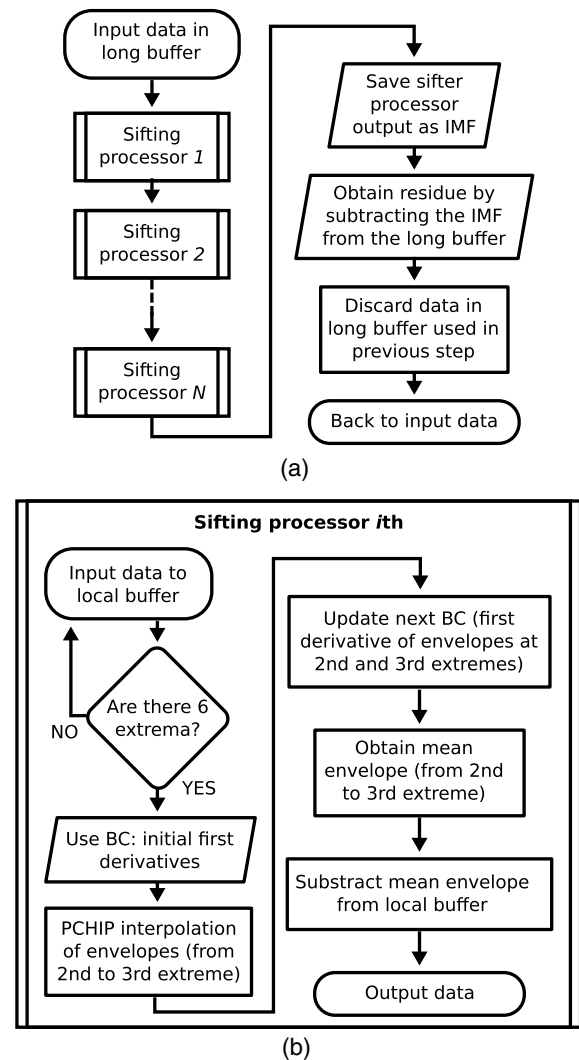

Fig. 3. Flowchart of the proposed real-time EMD algorithm using a cascade of sifting processors. (a) Complete algorithm, (b) flowchart of a single sifting processor.
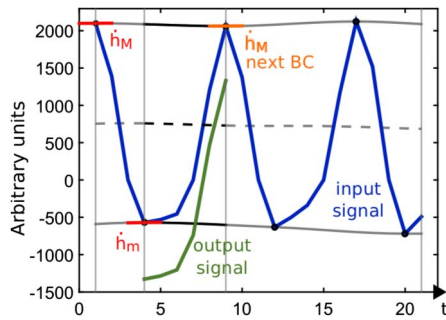
Fig. 4. Illustration of a single sifting processor applied to a generic signal.

Fig. 5. Illustration of the application of the operator $\mathcal{L}$ to a buffered generic signal.

C. Intrinsic Time-scale Decomposition

In this section we describe the intrinsic time-scale decomposition (ITD) filtering method, which is an adaptive algorithm for decomposing a signal into a sum of proper rotation components (PRC) and a trend [27]. Particularly, ITD preserves precise temporal information regarding critical signal points and riding waves with a temporal resolution equal to the time-scale of the occurrence of extrema in the input signal. ITD uses a non-iterative operator $\mathcal{L}$ that extracts a residual signal from a real function $s(t)$ in a way that $c_1(t) = [1 - \mathcal{L}s(t)]$ is a PRC with well-defined instantaneous frequency similar to the IMFs obtained by applying the EMD method. The piecewise linear-residual extracting operator is described as

$$\mathcal{L}s(t) \equiv L_t = L_k + \frac{L_{k+1} - L_k}{s_{k+1} - s_k}[s(t) - s_k], t \in (\tau_k, \tau_{k+1}], \quad (3)$$

where $\{\tau_k, k = 1, 2, \ldots\}$ are the local extrema of $s(t)$, $\tau_0 = 0$, $s_k = s(\tau_k)$, $L_k = L(\tau_k)$, and

$$L_{k+1} = \alpha\left[s_k + \frac{\tau_{k+1} - \tau_k}{\tau_{k+2} - \tau_k}(s_{k+2} - s_k)\right] + (1 - \alpha)s_{k+1}, \quad (4)$$

with $\alpha \in (0, 1)$ and typically fixed at $\alpha = 0.5$. Through this definition, L_t always remains inside the envelope described by the knots (τ_k, s_k). As L_t is a linear contraction of $s(t)$ even at inter-extrema intervals, it forces $c_1(t)$ to maintain the monotonicity of $s(t)$ between extrema, which is a necessity for PRCs. This way of defining PRCs allows a real-time recursive implementation that finds a new interval of PRC with the arrival of each new local extrema. The delay to achieve a PRC is limited to two extrema of $s(t)$. An illustration of the operator $\mathcal{L}$ applied to a generic buffered signal is shown in Fig. 5.

This process can be applied again to the residual signal $r_1(t) = L_t$ in order to decompose the original signal into a sequence of PRCs of successively decreasing rates of oscillation at each level j of the decomposition. More precisely, $r_j(t) = \mathcal{L}r_{j-1}(t)$ and $c_j(t) = \mathcal{H}\mathcal{L}^{j-1}s(t)$ where $\mathcal{H} = 1 - \mathcal{L}$. The procedure can be iterated until a monotonic trend is obtained.

The parameter α does not affect the instantaneous frequencies of the extracted PRC. Using a value of $\alpha < 0.5$, a PRC with lower energy is extracted from the input signal and a residual signal with the presence of information at the rapid time scale given by the occurrence of extrema at the input signal is obtained. Alternatively, setting $\alpha > 0.5$ makes $\mathcal{H}$ extract more energy of the fast activity from the input signal.
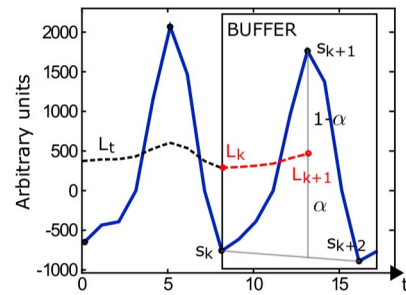
ITD can be used instead of EMD in step 4 of the algorithm of BivEMD shown in Sec. 2.B for defining a new TSPI phase-recovery method. The following notes the two main differences between BivEMD and ITD methods.

• ITD is computationally low-cost since no interpolation is performed during PRC extraction.
• ITD is a low delay replacement of BivEMD, especially when more than one BIMF is required for the phase-recovery procedure.
• Mislocalization of temporal information and distortions in the extracted components are minimized because intermediate residuals are not exclusively determined by the extrema of the original signal for $c_1(t)$ or $r_{j-1}(t)$ for $c_j(t)$ compared with the EMD method.

3. NUMERICAL RESULTS

In order to evaluate the performance of the three real-time phase-recovery methods previously proposed, several sequences of N_T frames, each one containing $N \times N$ intensity pixels of speckle interferograms, were generated using a simulation method previously used for the assessment of different phase-recovery algorithms [11,20]. Two different simulations were performed to analyze the performance of the methods: (1) The usual TSPI optical setup with a single camera, and (2) the SQHI optical setup by adding a second camera that acquires intensity images produced by the object arm with phase in quadrature (see Fig. 6 and also [18] for specific details of the optical setup and the mathematical description of the phase-recovery technique). In the SQHI technique the interferograms from different cameras are subtracted in order to suppress the background intensity from the analyzed sequence corresponding to the evolution of the object phase. Each single interferogram is generated by means of

$$I_1(m, n, t) = A^2|Re^{i[\zeta + \theta(t)]} + \mathcal{F}^{-1}\{H(u, v) \\ \times \mathcal{F}\{e^{i\phi_o(m,n,t)}U(m, n)\}\}|^2, \quad (5)$$

where A is the laser beam amplitude, R is a relation of amplitude between the reference and the object beams, ζ is the phase difference between the two beams, $\mathcal{F}\{\bullet\}$ and $\mathcal{F}^{-1}\{\bullet\}$ are the operators of 2D FFT and its inverse, respectively. The temporal carrier $\theta(t)$ is a periodic sequence with phase steps of $[0; \pi/2; \pi; 3\pi/2]$ radians sequentially. The spatio-temporal evolution of the object phase is represented by $\phi_o(m, n, t)$ with integers
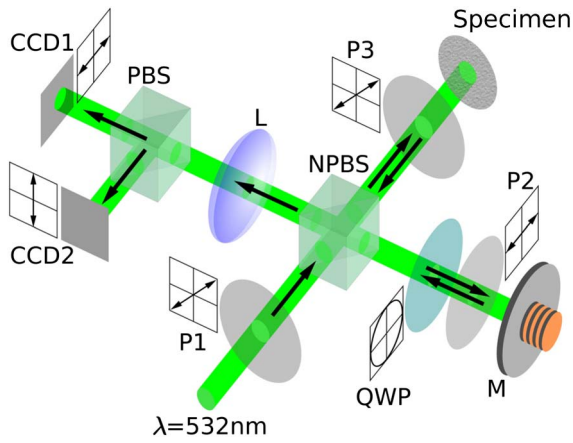
Fig. 6. Simultaneous $\pi/2$ phase-shifting heterodyne interferometer (SQHI) used in spatio-temporal object phase reconstruction. (CCD1) and (CCD2) detectors; (PBS) and (NPBS) polarized and non-polarized beam splitters, respectively; (QWP) $\lambda/4$ wave plate, specimen with optically rough surface; (M) piezo-electrically driven mirror; (P1, P2) polarizers; and (L) lens of focal length f. Interested readers, see [18] for specific details of the optical setup and the mathematical description of the phase recovery technique.

n, m, and t verifying the relationships $1 \leq m, n \leq N$ and $1 \leq t \leq N_T$. $U(m, n)$ is a matrix of random complex numbers with the phase uniformly distributed in the interval $[-\pi, \pi)$ radians and unitary amplitude. $H(u, v)$ denote a circular low-pass filter in the Fourier plane with radius $a \leq N/2$ that sets the average speckle size given by the relation $\rho_o = N/(2a)$. In this work we adopted $\rho_o = 1.1$ to ensure a proper simulation of small grains of speckle. The SQHI intensities I_{SQHI} were obtained by subtracting the quadrature version of the intensity images described by Eq. (5):

$$I_2(m, n, t) = A^2 |Re^{i\left[\zeta + \theta(t) + \frac{\pi}{2}\right]} + \mathcal{F}^{-1}\{H(u, v)$$
$$\times \mathcal{F}\{e^{i\phi_o(m,n,t)}U(m, n)\}\}|^2, \tag{6}$$

$$I_{\mathrm{SQHI}}(m, n, t) = I_2(m, n, t) - I_1(m, n, t). \tag{7}$$

The reference beam was simulated with a mean intensity six times larger than the spatial mean intensity of the object beam. Two main sources of noise were introduced to analyze the robustness of the tested phase-reconstruction methods. The inaccuracy and nonlinearity of the actuator that generated the carrier was simulated according to the expression

$$\theta(t) = t\frac{\pi}{2}[1 + \eta_C(t\%4)], \tag{8}$$

where $\eta_C(t\%4)$ is a repetitive phase error and the operator % is the remainder after division. The CCD readings $I_{\mathrm{CCD}}(m, n, t)$ were modeled by adding Gaussian noise images $\eta_{\mathrm{CCD}}(m, n, t)$ with standard deviation σ_{CCD} to the interferometric intensity signals $I(m, n, t)$:

$$I_{\mathrm{CCD}}(m, n, t) = I(m, n, t) + \eta_{\mathrm{CCD}}(m, n, t), \tag{9}$$

Subsequently, the resulting intensities were converted to eight-bit values to simulate the digitizing process in a low-resolution CCD sensor.

The spatio-temporal object phase evolution was assigned to all the pixels by generating a sequence of images following the relation

$$\phi_o(m, n, t) = K_E \phi_{sp}(m, n)\delta(t), \tag{10}$$

where $\delta(t)$ is a 1D temporal sequence of phase steps with damped oscillation [see black solid curve in Fig. 7(a)]. The spatial-phase distribution corresponding to the deformation $\phi_{\mathrm{sp}}(m, n)$ was selected as shown in Fig. 8(a). The parameter K_E allows us to easily simulate different amplitudes of object-phase variations by keeping $\phi_{\mathrm{sp}}(m, n)$ and $\delta(t)$ unchanged. Note that the extreme value of $\phi_{\mathrm{sp}}(m, n)$, the height of a single step in $\delta(t)$ and K_E set the maximum excursion of the phase evolution $\hat{E}_\phi = \max_{m,n}[E_\phi(m, n)]$ with pixel excursions $E_\phi(m, n) = \max_{t\in ss}[\phi_o(m, n, t)] - \min_{t\in ss}[\phi_o(m, n, t)]$. We used the notation $\max_k[\bullet(k)]$ as the maximum $\bullet(k)$ for all valid arguments k and ss is the time interval of a single step. This choice of $\phi_o(m, n, t)$ gives very dissimilar temporal phase variations within the same field of analysis.

The solid-black curve in Fig. 7 shows $\phi_o(t)$ at an arbitrarily selected pixel and it is compared with the evolution of the unwrapped recovered phase for the methods of digital filtering based on a tenth order Butterworth filter (DFM-Butter), real-time BivEMD with PCHIP interpolation, and ITD when one or two BIMFs and PRCs were eliminated in the last two methods. In Fig. 7 we show the evolution of the reconstructed phase for two cases of excursion and levels of noise given by K_E and σ_{CCD} variations, generating a sequence of SNR = 23 dB [Fig. 7(a)] and others of SNR = 10 dB [Fig. 7(b)]. In the high
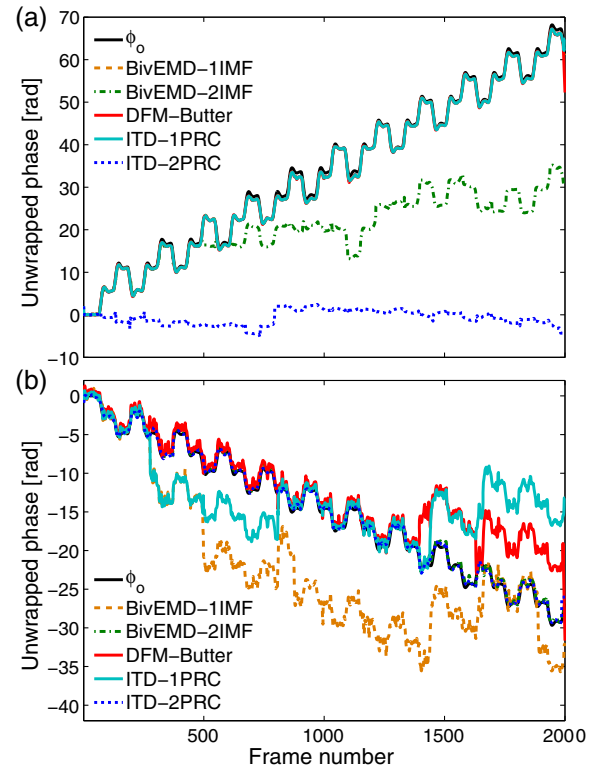

Fig. 7. Original and reconstructed temporal evolution of phase at a given pixel for a simulated sequence of interferograms: (a) SNR = 32 dB and (b) SNR = 10 dB.
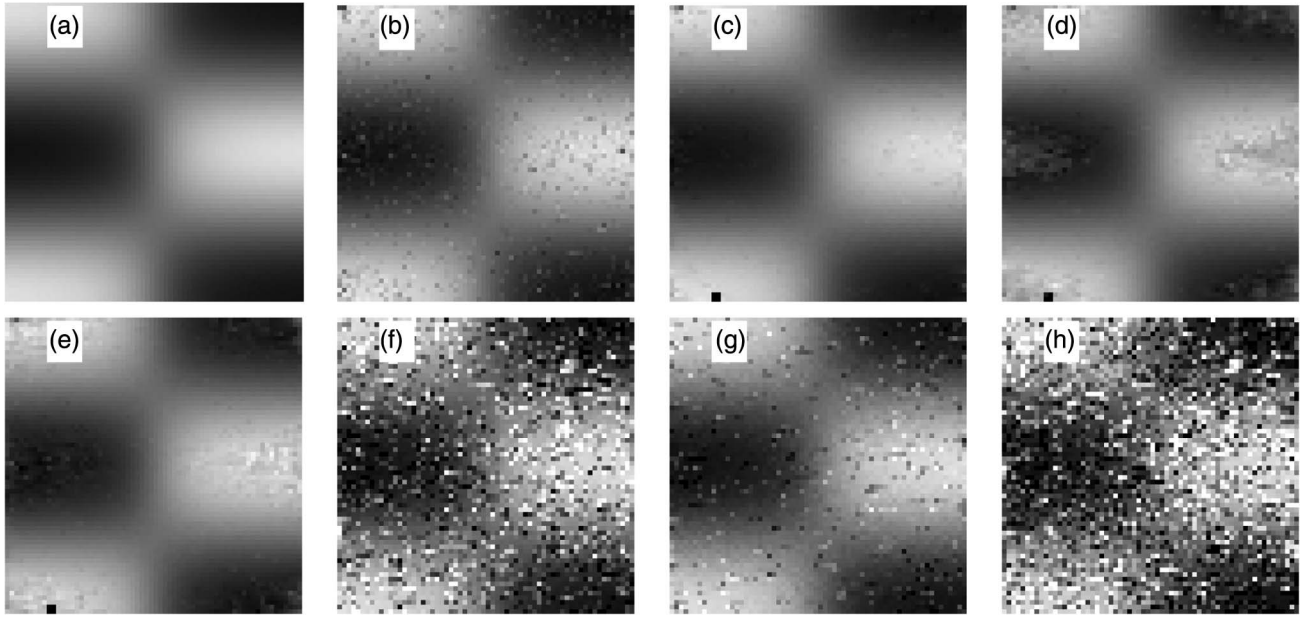
Fig. 8. (a) Simulated $\phi_o(m, n, 1000)$, 64×64 pixels spatial distribution of the object phase at frame 1000 (original phase). Spatial distribution of reconstructed phase at frame 1000 for the cases (b)–(e) $\hat{E}_\phi = 29.7$ rad and SNR = 23 dB; grayscale from –100 (white) to 100 (black); (f)–(h) $\hat{E}_\phi = 5.6$ rad; and SNR = 10 dB; grayscale from –19 (white) to 19 (black). (b) BivEMD-1IMF unfiltered, (c) Delaunay triangulation filtering (DTF) for (b), (d) DFM-Butter with DTF, (e) ITD-1PRC with DTF, (f) ITD-1PRC with DTF, (g) ITD-2PRC with DTF, (h) DFM-Butter with DTF.

SNR case, DFM-Butter, BivEMD-1IMF and ITD-1PRC proved to recover the correct high-excursion phase evolution. In Fig. 7(b), a low-excursion phase evolution was simulated and noise levels achievable with usual cameras and exposure times were used to test the methods in the case of having a more demanding environment or low-quality acquisition equipment. It is seen that the resulting phase evolutions show higher errors. BivEMD-2IMF and ITD-2PRC reconstructed the correct phase evolution showing no disengagements for this particular pixel. Below we present a more complete characterization of the performance given by these methods.

The spatial distortion of the phase images between the original object phase ϕ_o and the recovered phase ϕ_o^{est} was analyzed by using the structural similarity (SSIM) index [28]. A quality factor $Q(t)$ is obtained at each frame t in the range of values [–1, 1], where $Q(t) = 1$ is satisfied for an exact phase reconstruction. By using a sliding window approach, for every spatial translation j, $Q_j(t)$ is calculated locally by means of the relation

$$Q_j = \frac{2(2\overline{\phi_o}\,\overline{\phi_o^{est}} + C_Q)(\sigma_{\phi_o\phi_o^{est}} + C_Q)}{(\overline{\phi_o}^2 + \overline{\phi_o^{est2}} + C_Q)(\sigma_{\phi_o}^2 + \sigma_{\phi_o^{est}}^2 + 2C_Q)}, \quad \textbf{(11)}$$

where σ_{ϕ_o} and $\sigma_{\phi_o^{est}}$ are standard deviations of ϕ_o and ϕ_o^{est}, respectively., $\sigma_{\phi_o\phi_o^{est}}$ is the correlation coefficient between ϕ_o and ϕ_o^{est}, $\overline{\phi_o}$ and $\overline{\phi_o^{est}}$ are the means of both portions of the images, and the fixed constant $C_Q = 0.01$ avoids numerical instability. Note that the number of frame dependence was omitted for clarity. The SSIM index $Q(t)$ is obtained by calculating the average of all local $Q_j(t)$.

In Fig. 8(a) we show the spatial distribution of the unwrapped original object phase $\phi_o(m, n, 1000)$ at frame 1000, adopting $\hat{E}_\phi = 29.7$ rad. The numerical values of phase are

represented from white to black in grayscale for the interval [–100, 100] rad. Figure 8(b) presents the phase reconstructed by the BivEMD-1IMF method for the SNR = 23 dB case at frame 1000 using PCHIP for envelope interpolation. A dynamic regime Delaunay triangulation filtering (DTF) method presented in [29] was applied to the recovered sequence of images for removing noisy pixels due to low-modulated speckle. A simple moving average filter of the absolute value of the temporal variations of intensity was used as an indicator of reliability of each pixel and a hysteresis thresholding process allowed us to discard results from entire temporal blocks of low-modulated pixels and replace them by interpolating the recovered object phase from reliable neighboring pixels. In Fig. 8(c) we show the DTF filtered result of BivEMD-1IMF method from Fig. 8(b). The SSIM index obtained for the image in Fig. 8(b) was $Q = 0.77$ and the filtered result in Fig. 8(c) obtained $Q^{DTF} = 0.94$. In Figs. 8(d) and 8(e), we show the resulting phase images by using DFM-Butter and ITD-1PRC with DTF obtaining $Q^{DTF} = 0.77$ and $Q^{DTF} = 0.85$, respectively. In Figs. 8(f)–8(h) the DTF results for ITD-1PRC, ITD-2PRC, and DFM-Butter are sequentially shown for direct visual comparison of the recovered phase images at frame 1000 by using low excursion $\hat{E}_\phi = 5.6$ rad and SNR = 10 dB. The values of phase were represented from white to black in grayscale for the interval [–19, 19] rad. The obtained SSIM indices were $Q^{DTF} = 0.1$ for ITD-1PRC, $Q^{DTF} = 0.52$ for ITD-2PRC and $Q_b^{DTF} = 0.51$ for DFM-Butter. ITD-2PRC obtained cleaner images, presenting a low amount of phase disengagements and higher accuracy of phase recovery.

Figure 9 depicts the temporal evolutions of the SSIM index computed for the two analyzed cases corresponding to a single camera setup. These results correspond to the average SSIM
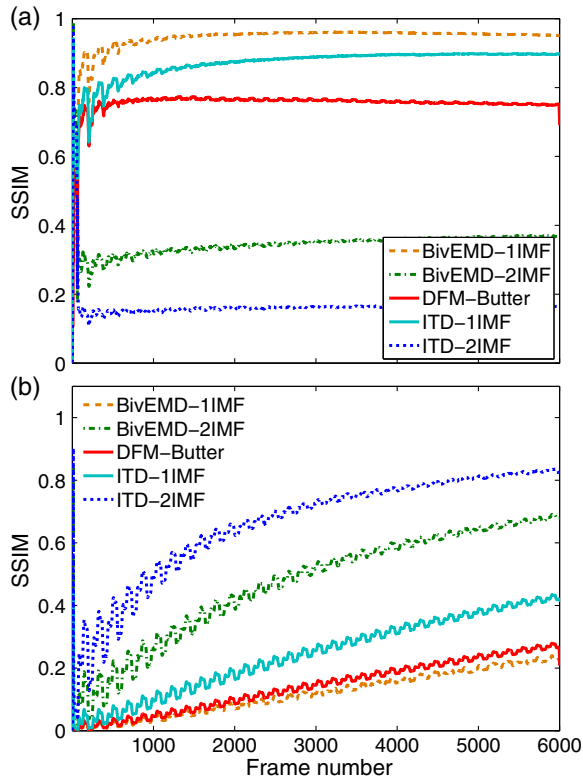
(a)

(b)

Fig. 9. Temporal evolution of the SSIM index for the reconstructed and filtered phases when a single camera TSPI is simulated and with (a) $\hat{E}_\phi = 29.7$ rad and SNR = 23 dB, (b) $\hat{E}_\phi = 5.6$ rad and SNR = 10 dB.

indices obtained from an ensemble of 15 simulations for each excursion and SNR values. BivEMD-1IMF and ITD-1PRC proved to be the best methods to reconstruct the phase in the high-excursion and low-noise case. The extraction of two IMFs in these two methods is not recommended for high excursion of the phase evolutions. However, ITD-2PRC and BivEMD-2IMF gave the best performance for the set of low excursions.

We used C implementations for the tested methods, which were interfaced with MATLAB scripts and processed in a 2.93 GHz Central Processing Unit (CPU). An offline processing of TSPI sequences with $N = 64$ and $N_T = 6000$ allowed estimation of the maximum input-frame rate for every method in a scheme that does not present the idle times that occur in a real-time situation when the algorithm waits for new frames. The average elapsed times for this particular nonreal-time tests were: 25 s for BivEMD-1IMF (implying a processing rate of 4.2 ms/frame), 61 s for BivEMD-2IMF (10.2 ms/frame), 15 s for DFM-Butter (2.5 ms/frame), and 18 and 22 s (3 and 3.7 ms/frame) for ITD when extracting one PRC and two PRCs, respectively. The results show that the DFM-Butter and the ITD-1PRC analysis are the fastest phase-reconstruction methods and BivEMD-2IMF is considerably slower than the other approaches. The elapsed times indicate that an analysis frame rate of 240 frames per second can be achieved by using BivEMD-1IMF, ITD-1PRC, and DFM-Butter.

Table 1 shows the SSIM indices at frame 5500 where there is no temporal-border effect and the initial transient state of the

Table 1. SSIM Index at Frame 5500 for Single Camera TSPI

E_ϕ [rad]	5.6		13.0		29.7	
	SNR [dB]					
Method	**23**	**10**	**23**	**10**	**23**	**10**
BivEMD-1IMF	0.98	0.22	0.98	0.51	0.95	0.57
BivEMD-2IMF	0.98	0.67	0.84	0.60	0.37	0.19
DFM-Butter	0.98	0.25	0.98	0.54	0.75	0.44
ITD-1PRC	0.98	0.40	0.98	0.64	0.89	0.47
ITD-2PRC	0.98	0.82	0.44	0.37	0.17	0.11

SSIM evolution has been practically completed. An intermediate excursion case ($\hat{E}_\phi = 13$ rad) is added to this table. Note that the SSIM indices for the low-noise situation are high for every method except for the high-excursion case where BivEMD-1IMF and ITD-1PRC performed better than the rest of the other approaches. In the case of $\hat{E}_\phi = 5.6$ rad and low SNR, ITD-2PRC proved to be the best tuned method. The robustness of the BivEMD-1IMF method to different sources of noise is exhibited in the SSIM index results for the highest excursion case.

The real-time implementation of the classical FT technique based on digital filtering was a simple and efficient option for an initial treatment of single camera TSPI images, especially for knowing the range of phase excursions within the field-of-view. However, the best accuracy in-phase reconstruction was obtained by the BivEMD and ITD methods. We recommend the
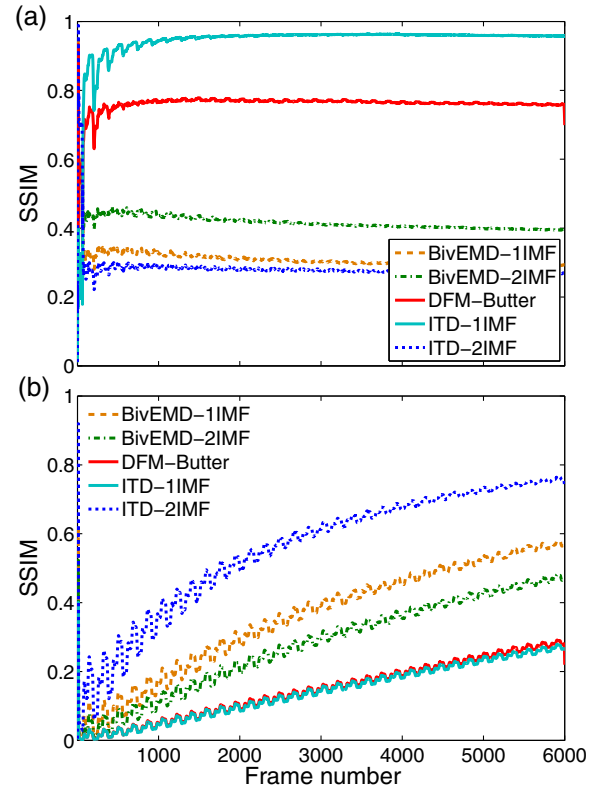
(a)

(b)

Fig. 10. Temporal evolution of SSIM index for the reconstructed and filtered phases for the simulations of SQHI with (a) $\hat{E}_\phi = 29.7$ rad and SNR = 23 dB, (b) $\hat{E}_\phi = 5.6$ rad and SNR = 10 dB.

Table 2. SSIM Index at Frame 5500 for TSPI-SQHI

E_ϕ [rad]	5.6		13.0		29.7	
	SNR [dB]					
Method	23	10	23	10	23	10
BivEMD-1IMF	0.98	0.55	0.94	0.68	0.29	0.23
BivEMD-2IMF	0.98	0.45	0.98	0.66	0.40	0.26
DFM-Butter	0.98	0.27	0.98	0.55	0.76	0.45
ITD-1PRC	0.97	0.25	0.98	0.53	0.96	0.56
ITD-2PRC	0.98	0.75	0.84	0.60	0.27	0.18

use of ITD-2PRC for a low-excursion and low-SNR situation, and BivEMD-1IMF for high-excursion independent of the level of noise in the image acquisition. The fast and simple ITD-1PRC method can also be used for an initial inspection of the phase distribution.

The analysis was also performed for simulated SQHI images. Figure 10 shows the SSIM index evolution obtained for the same two SNR and excursion cases. Table 2 shows the obtained results for the equivalent set of SSIM indices at frame 5500 as it was characterized in Table 1 for single camera TSPI. The SQHI BivEMD method has shown a lower performance in comparison with the other approaches regarding noise robustness. However, it is still preferable in its application for medium-excursion phase evolutions. From the results of Fig. 10 and Table 2, it is clear that ITD becomes the best choice for low- and high-excursion cases.

In TSPI-SQHI, ITD-1PRC should be used to know the range of excursions and a second PRC should be extracted for phase distributions with low excursion. BivEMD also yields high-quality phase maps and higher processing times. We recommend the use of SQHI to obtain more accurate phase maps in cases of high-phase excursion rates, especially with low SNR.

4. EXPERIMENTAL RESULTS

Real-time phase-reconstruction methods were implemented on a SQHI optical setup, which is based on a Twyman–Green interferometer as described in [18]. In this setup, two simultaneous temporal carriers with $\pi/2$ phase difference and orthogonal polarizations are obtained by selecting the orientation of a properly positioned analyzer (see Fig. 6). An exponentially decaying voltage signal was applied to a PZT disk and the deforming surface of one electrode of the disk was used as the specimen with dynamic deformations. A set of SQHI intensity
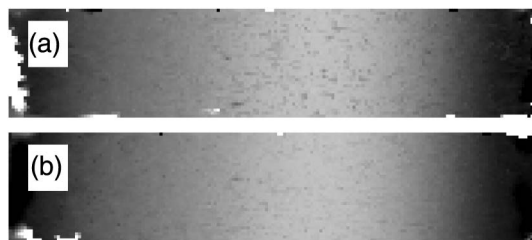
Fig. 11. (a) Displacement fields recovered by ITD-2PRC (with DTF) at frame 1800 of the experimental sequence of interferograms for a single camera TSPI and (b) SQHI setup. Grayscale images with values ranging from 0 (black) to 17 μm (white).
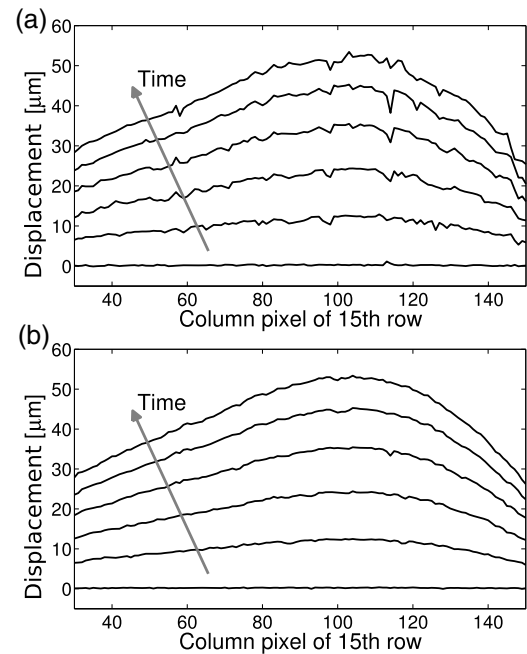
Fig. 12. Profiles of displacements given by BivEMD-1IMF (with DTF) at six different time instants. (a) Frames from 50 to 8294, spaced at intervals of 1650 frames for a single camera TSPI and (b) SQHI setup.

images corresponding to a sequence of 9216 images for each polarization was acquired to measure the real-time out-of-plane displacement field over a strip-shaped region that crosses the surface of the PZT device. Note that a single-camera TSPI can be adopted by recording a single sequence corresponding to a particular election of the light polarization.

A representative displacement field generated by the PZT disk at frame 1800 of the TSPI sequence obtained by ITD-2PRC with DTF is shown in Fig. 11(a). As expected, the brighter zone of the image corresponds to the center of the PZT disk where the vertical displacement of the surface is maximum.
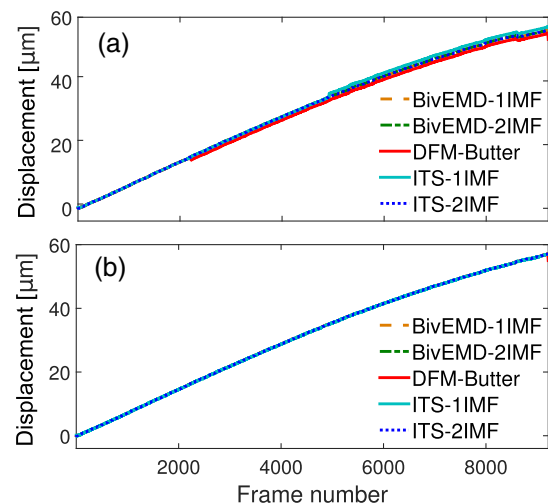
Fig. 13. Temporal evolution of the displacement field given by the five tested methods at a particular pixel for (a) single camera TSPI and (b) SQHI setup.

Figure 11(b) highlights a cleaner result given by the SQHI setup for the same conditions of Fig. 11(a). In Fig. 12 the out-of-plane displacement evolution at a particular pixel row is depicted for the results obtained with BivEMD-1IMF. Again, the results given by the SQHI setup show less noise than the single-camera TSPI. Finally, the unfiltered temporal evolution of the displacement recovered by the five methods at a single pixel is presented in Fig. 13 for single-camera TSPI and SQHI technique.

5. CONCLUSIONS

Real-time TSPI phase-recovery methods allow measurement systems usable for *in situ* nondestructive testing and offer an extra measurement advantage when compared with common post-processing techniques. Three different real-time methods were successfully implemented and applied on sequences of simulated and experimental speckle-pattern interferograms for comparison purposes. Two different TSPI optical setups were analyzed for the performance evaluation of the methods to be used on different intensity signals. The ITD provided a technique for nonlinear and nonstationary analysis and filtering, useful for real-time phase-reconstruction processing using the same approach as in BivEMD TSPI method and more especially for SQHI technique. The simple analysis given by the real-time digital-filtering method allows us to perform an initial treatment of single-camera TSPI images for rapid insight of dynamic specimens. The best accuracy in phase reconstruction was obtained by the adaptive analysis of BivEMD and ITD methods. In a single-camera TSPI scheme, we recommend the use of ITD-2PRC for a low-excursion situation and BivEMD-1IMF for high excursion. In TSPI-SQHI, ITD-1PRC should be used to know the range of excursions and a second PRC should be extracted for phase distributions with low excursion. The assessment of the intensity modulation and the posterior phase interpolation at low-modulated pixels based on Delaunay triangulation allows maintaining the performance of the phase-recovery methods for all pixels even after a temporal interval of low modulation.

REFERENCES

1. W. Osten, *Optical Inspection of Microsystems* (CRC Press, 2006).
2. G. Pedrini, J. Gaspar, M. E. Schmidt, I. Alekseenko, O. Paul, and W. Osten, "Measurement of nano/micro out-of-plane and in-plane displacements of micromechanical components by using digital holography and speckle interferometry," Opt. Eng. **50**, 101504 (2011).
3. L. Cavallini, G. Bolognesi, and R. Di Leonardo, "Real-time digital holographic microscopy of multiple and arbitrarily oriented planes," Opt. Lett. **36**, 3491–3493 (2011).
4. W. Osten and N. Reingand, *Optical Imaging and Metrology: Advanced Technologies* (Wiley, 2012).
5. S. Knoche, B. Kemper, G. Wernicke, and G. von Bally, "Modulation analysis in spatial phase shifting electronic speckle pattern interferometry and application for automated data selection on biological specimens," Opt. Commun. **270**, 68–78 (2007).
6. S. K. Debnath and Y. Park, "Real-time quantitative phase imaging with a spatial phase-shifting algorithm," Opt. Lett. **36**, 4677–4679 (2011).
7. J. Burke and H. Helmers, "Spatial versus temporal phase shifting in electronic speckle-pattern interferometry: noise comparison in phase maps," Appl. Opt. **39**, 4598–4606 (2000).
8. C. Joenathan, P. Haible, and H. J. Tiziani, "Speckle interferometry with temporal phase evaluation: influence of decorrelation, speckle size, and nonlinearity of the camera," Appl. Opt. **38**, 1169–1178 (1999).
9. C. Coggrave and J. Huntley, "Real-time visualisation of deformation fields using speckle interferometry and temporal phase unwrapping," Opt. Laser Eng. **41**, 601–620 (2004).
10. C. Joenathan, B. Franze, P. Haible, and H. Tiziani, "Speckle interferometry with temporal phase evaluation for measuring large-object deformation," Appl. Opt. **37**, 2608–2614 (1998).
11. G. H. Kaufmann, "Phase measurement in temporal speckle pattern interferometry using the Fourier transform method with and without a temporal carrier," Opt. Commun. **217**, 141–149 (2003).
12. Y. Fu, C. J. Tay, C. Quan, and H. Miao, "Wavelet analysis of speckle patterns with a temporal carrier," Appl. Opt. **44**, 959–965 (2005).
13. A. Federico and G. H. Kaufmann, "Robust phase recovery in temporal speckle pattern interferometry using a 3D directional wavelet transform," Opt. Lett. **34**, 2336–2338 (2009).
14. V. Madjarova, H. Kadono, and S. Toyooka, "Dynamic electronic speckle pattern interferometry (despi) phase analyses with temporal Hilbert transform," Opt. Express **11**, 617–623 (2003).
15. G. Rilling, P. Flandrin, and P. Gonalves, "On empirical mode decomposition and its algorithms," *IEEE-EURASIP Workshop on Nonlinear Signal and Image Processing (NSIP)*, Grado, Italy, 2003.
16. F. A. M. Rodriguez, A. Federico, and G. H. Kaufmann, "Hilbert transform analysis of a time series of speckle interferograms with a temporal carrier," Appl. Opt. **47**, 1310–1316 (2008).
17. S. Equis and P. Jacquot, "The empirical mode decomposition: a must-have tool in speckle interferometry?" Opt. Express **17**, 611–623 (2009).
18. A. Bianchetti, F. E. Veiras, P. Etchepareborda, A. L. Vadnjal, A. Federico, and G. H. Kaufmann, "Amplitude and phase retrieval in simultaneous π/2 phase-shifting heterodyne interferometry using the synchrosqueezing transform," Appl. Opt. **54**, 2132–2140 (2015).
19. A. Oppenheim and R. Schafer, *Digital Signal Processing* (Prentice-Hall, 1991).
20. P. Etchepareborda, A. Bianchetti, A. Vadnjal, A. Federico, and G. Kaufmann, "Simplified phase-recovery method in temporal speckle pattern interferometry," Appl. Opt. **53**, 7120–7128 (2014).
21. G. Rilling, P. Flandrin, P. Gonalves, and J. Lilly, "Bivariate empirical mode decomposition," IEEE Signal Process. Lett. **14**, 936–939 (2007).
22. A. Eftekhar, C. Toumazou, and E. M. Drakakis, "Empirical mode decomposition: Real-time implementation and applications," J. Signal Process. Syst. **73**, 43–58 (2013).
23. A. Santillan-Guzman, M. Fischer, U. Heute, and G. Schmidt, "Real-time empirical mode decomposition for EEG signal enhancement," in *Proceedings of the 21st European Signal Processing Conference (EUSIPCO)* (IEEE, 2013), pp. 1–5.
24. A. Zeiler, R. Faltermeier, A. M. Tomé, C. Puntonet, A. Brawanski, and E. W. Lang, "Weighted sliding empirical mode decomposition for online analysis of biomedical time series," Neural Process. Lett. **37**, 21–32 (2013).
25. S. A. Bagherzadeh and M. Sabzehparvar, "A local and online sifting process for the empirical mode decomposition and its application in aircraft damage detection," Mech. Syst. Signal Proc. **54**, 68–83 (2015).
26. F. R. Holzinger and M. Benedikt, "Online instantaneous frequency estimation utilizing empirical mode decomposition and Hermite splines," in *2013 Proceedings of the 22nd European Signal Processing Conference (EUSIPCO)* (IEEE, 2014), pp. 446–450.
27. M. G. Frei and I. Osorio, "Intrinsic time-scale decomposition: time-frequency-energy analysis and real-time filtering of non-stationary signals," Proc. R. Soc. A **463**, 321–342 (2007).
28. Z. Wang, A. Bovik, H. Sheikh, and E. Simoncelli, "Image quality assessment: from error visibility to structural similarity," IEEE Trans. Image Process. **13**, 600–612 (2004).
29. S. Equis, "Phase extraction of non-stationary signals produced in dynamic interferometry involving speckle waves," Ph.D. thesis (École Polytechnique Fédérale de Lausanne, 2009).